Nuclear Instruments and Methods in Physics Research B 531 (2022) 34–43

Contents lists available at ScienceDirect

Nuclear Inst. and Methods in Physics Research, B

journal homepage: www.elsevier.com/locate/nimb

Collector-based measurement of gas desorption and secondary electron emission induced by 0–1.4 keV electrons from LHC-grade copper at 15 K

Michal Haubner [a,b,*], Vincent Baglin [b], Bernard Henrist [b]

[a] Department of Physics, Faculty of Mechanical Engineering, Czech Technical University in Prague, Czech Republic
[b] European Organization for Nuclear Research (CERN), Geneva, Switzerland

ARTICLE INFO

Keywords:
Electron stimulated desorption
Secondary electron yield
Electron conditioning
Technical surface
Cryogenic temperatures
Feulner cap

ABSTRACT

CERN's Large Hadron Collider cryomagnets embed a 1.9 K UHV chamber lined with a 5–20 K beam-screen (BS) that intercepts the synchrotron radiation and electron cloud (EC). The low–energy EC irradiates the BS and desorbs gas, creating a dynamic vacuum effect. A novel setup controllably reproduces this by irradiating an unbaked as-received BS copper sample at 15 K with 0–1.4 keV electrons, representing a slice of the EC spectrum. This collector-based setup is qualified using a HOPG reference for secondary electron yield (SEY) and $^{15}N_2$ as a tracer in low-energy electron stimulated desorption (ESD) measurements. Measurement at 15 K revealed sub-10 eV ESD thresholds and a maximum around 300 eV of 0.18 H_2/e^- and 0.13 CO/e^-. Irradiation with 300 eV and 1 keV electrons at ~ 8.10^{-4} C.mm^{-2} conditioned ESD and SEY alike. Similar dose at 17 eV only caused minor SEY reduction and no ESD decline. The as-received H_2 and CO_2 yields at 300 eV decreased 5-150x between 15 and 265 K, respectively..

1. Introduction

In storage rings, accelerators and light sources, the circulating charged particle beam may provoke a large pressure increase by up to five orders in magnitude above the base pressure. This dynamic pressure rise, potentially limiting the machine's performance, has been long observed in room temperature machines but only recently at cryogenic temperatures in the CERN's Large Hadron Collider (LHC) [1], or the Relativistic Heavy Ion Collider, RHIC in the USA [2]. Large accelerators are designed considering the dynamic vacuum effect. This includes machines currently under construction, such are the electron–ion collider, eRHIC [3] or the heavy ion synchrotron SIS100 in Germany [4], as well as the next large colliders such as Future Circulars Colliders (FCC-ee and FCC-hh) in Europe [5,6] and the Circular Electron Positron Collider, CEPC, or Super Proton-Proton Collider, SPPC in China [7]. This effect is mainly attributed to non-thermal gas desorption stimulated by particles, such as photons, electrons, ions and beam-loss particles, impinging on the inner surface of a vacuum vessel. In particular, the electron stimulated desorption (ESD) is of major importance for modern machines that exhibit electron cloud (EC), a phenomenon originating from closely spaced dense bunched beams.

The LHC is a proton storage ring of 27 km circumference designed to collide proton beams at 14 TeV in the centre of mass [8]. It consists of superconducting magnets with a 1.9 K cold bore. A beam–screen (BS) cooled to 5–20 K, is inserted into the cold bore to extract the heat generated by the circulating beam via resistive wall heating, synchrotron radiation (SR) and by electron cloud (EC) [9,10]. At the nominal beam energy of 7 TeV, the relativistic proton beam emits synchrotron radiation of 44 eV critical energy that is intercepted by the BS. As observed during the beam energy ramp-up above 2 TeV [1], the energy of the emitted SR photons surpasses the ~4 eV work function of the copper surface to extracts photoelectrons. Slow photoelectrons are then accelerated by the electric field of the passing proton bunches [11], impinge on the beam-screen surface again, multipact and form an EC [12]. Under the conditions when the EC prevails, a self-sustaining electron population continuously irradiates the BS surface, desorbing gas. The closed geometry of the beam tube inherently limits the pumping speed and makes the gas sources mitigation even more important. Similar to room temperature machines, while operating the LHC, the electron-cloud activity and the dynamic vacuum diminish [1], a phenomenon systematically observed during LHC's Run 1 [13–17] and Run 2 [18,19]. This is due to the decrease of the secondary electron yield (SEY) and the surface conditioning (decrease of ESD) under electron bombardment. As a result, the dynamic vacuum effect gradually

* Corresponding author at: European Organization for Nuclear Research (CERN), Geneva, Switzerland.
E-mail address: michal.haubner@cern.ch (M. Haubner).

https://doi.org/10.1016/j.nimb.2022.09.013
Received 7 July 2022; Received in revised form 7 September 2022; Accepted 14 September 2022
Available online 30 September 2022

attenuates with operation time to an acceptable level but remains a concern when pushing up the accelerators' performance [20]. During the LHC commissioning, this non-thermal electron desorption mechanism was confirmed as the predominant gas source. Hence, the relationship between EC and the dynamic pressure rise calls for a systematic investigation, as it plays a crucial role in an effective operation of the LHC and its upcoming high-luminosity upgrade, the HL–LHC [21].

Available problematics overviews [22], including simulations [23] and even recent measurements [24] taken on the LHC's long straight sections, have shown that the electrons energy distribution of an EC resides mainly in the low energy, with a major peak below 10 eV and half of the population below ~20 eV. When the EC establishes a stable population, the major peak of secondary electrons is followed by a minor peak of beam-accelerated electrons at hundreds of eV. This electron energy distribution indeed varies with the actual beam parameters and the geometry, magnetic fields and surface state of the beam-screen. Therefore, we have designed an experimental setup to investigate material samples representative of the LHC's beam screen under the conditions it experiences in LHC cryomagnets. The setup controllably reproduces the relevant conditions in terms of: cryogenic temperatures under 20 K, ultrahigh vacuum in the 10^{-11} mbar range and low-energy and high-dose electron irradiation. Our present research focuses on developing a new measurement procedure to study the ESD and SEY in the sub-keV energy region at cryogenic temperatures, which is particularly relevant for the dynamic vacuum effect, but equally experimentally challenging.

Technical-grade metal surfaces are prevalent in industrial-scale installations, such as particle accelerators and impose a technical challenge due to their ill-defined surface state. Indeed, the employed UHV-grade cleaning procedures effectively reduce outgassing, both thermal and stimulated, as demonstrated by Mathewson [25]. Still, a technical surface exhibits statistical nature in terms of crystal orientation, chemical composition, oxide layer thickness, micro-porosity and texture, due to various air–exposure times, contamination, stains and batch-to-batch variation, differences in machining, cleaning and storage. The hereafter investigated surface was sampled from an LHC-grade metal sheet; an industrially produced technical-grade polycrystalline oxygen-free electronic "OFE" copper colaminated onto a stainless-steel sheet and thermally treated to 900 °C in a H_2 atmosphere. After cutting, the copper sample was cleaned for UHV in a warm ultrasonically agitated isopropanol bath, packaged in a plastic foil and then briefly exposed to an atmospheric air prior to insertion into the UHV chamber via a load-lock system. Hence, we study copper sample in an unbaked as–received surface state, as it is in the LHC cryomagnets.

2. Material and methods

2.1. Setup description

The experimental setup developed to study the ESD and SEY at cryogenic temperatures mainly consists of a μ–metal vacuum chamber, a 4-axis cryomanipulator, a low-energy electron gun and a quadrupolar mass spectrometer (QMS) fitted inside a collector. The setup is further equipped with a storage chamber and a load-lock chamber to introduce unbaked samples into the baked experimental chamber, allowing us to study the LHC BS in its actual as received unbaked surface state.

The vacuum chamber is constructed of μ–metal that shields off stray magnetic fields by a factor of 100, preventing deviation of the primary electron beam and altering trajectories of low-energy secondary electrons. A base pressure in the ultra-high vacuum (UHV) range of 10^{-11} mbar is achieved by a combination of turbomolecular, getter-cartridge vacuum pumps, cryo-pumping and a bakeout to 150 °C for 3 days. This ensures a monolayer (ML) formation time in the range of hours, such that the studied cold surface is not altered during a measurement, e.g. not altered following cryosorption of residual gas from the background.

The studied flag-type sample is inserted into the cryomanipulator which uses an open-cycle liquid He circuit that is vibration-free and capable of approaching a temperature of 10 K, as measured by a diode sensor mounted directly inside the sample holder. The sample holder is mounted onto the cryostat via a sapphire plate for a good thermal contact but electrical insulation, allowing the sample biasing and current measurement. The cryostat itself goes below 5 K, generating a strong cryopumping effect that reduces the base pressure from 10^{-10} to 10^{-11} mbar range.

A Kimball ELG-2 electron gun is used to imitate a monoenergetic slice of the energy spectrum of the LHC's electron cloud, allowing us to decouple contributions of different primary electron energies. According to specifications, the gun provides a stable, focused (<1 mm^2), monoenergetic ($\Delta E < 1$ eV), low energy (2 eV – 2 keV) and low intensity (0.1 nA – 10 μA) analytical beam. The electron gun is equipped with a Faraday cup (FC) for a direct current measurement of the emitted electrons. The focused beam irradiates the studied sample with perpendicular incidence from a focal distance of ~ 5 cm through circular openings in the collector.

As schematized in Fig. 1, the setup features a collector tube made of 0.1 mm thick stainless-steel sheet custom-designed to contain the secondary electrons and desorbed gas species. The collector geometry composes of a 75 mm wide and 750 mm long tube with an QMS on one side and an endcap on the opposite side. The endcap has two concentric 4 mm diameter openings that are in a line of sight with the e^- gun nozzle, allowing the primary electron beam to reach the studied sample. The closed geometry formed by the collector positioned 0.25 mm from the sample effectively captures most of the emitted and backscattered secondary electrons, which we have evidenced experimentally and by simulation. Both the sample and collector are electrically insulated from the ground (>100 GΩ at 500 V_{DC}), by a sapphire plate and a ceramic interpiece, to allow biasing and net current measurement of electrons arriving and leaving the system. Electric battery cells are used to bias the sample, chosen for their long-term stability and low intrinsic dark current. The collector is held at the ground potential for all experiments, whereas the sample bias V_S is set at −28 V for all energy-dependent SEY & ESD measurements and at +46 V for electron conditioning measurements using monoenergetic beams. The sole exception is conditioning using low-energy electrons, where a retarding bias set at −28 V is required to reach such low energies. For electron energies above 70 eV, the +46 V bias has the advantage of smaller dynamic background at the expense of no simultaneous SEY measurement.

The SEY is measured solely via the electron currents captured on the sample and collector. However, the ESD yield measurement can be subdivided into the current measurement of the primary electron beam and the measurement of the desorbing gases. For clarity, these will be treated separately, starting with the beam current measurement followed by a SEY measurement of Highly Oriented Pyrolytic Graphite (HOPG) reference sample.

2.2. Beam current measurement

The closed geometry of the sample–collector system effectively forms a Faraday cup, so that the sample current I_S and the collector current I_C sum up to the primary electron beam current I_B that interacts with the studied surface. The nozzle of the electron gun is also equipped with a rotating Faraday cup, whose reading equals to the net current gathered by the sample–collector system across the investigated energy range. The data acquisition (DAQ) chain consists of two Keithley 428 ammeters that typically provide a gain of 10^6 V/A and 10^9 V/A for ESD and SEY measurements, respectively. We use a built-in function of 100 ms integration time to suppress noise before directing the amplified signal into a DAQ card with a 16-bit wide A/D converter. The proper calibration and the nominal current reading are regularly verified across the DAQ chain. Coherent current reading across our system, from the e-gun Faraday cup to the sample–collector system, is also checked regularly

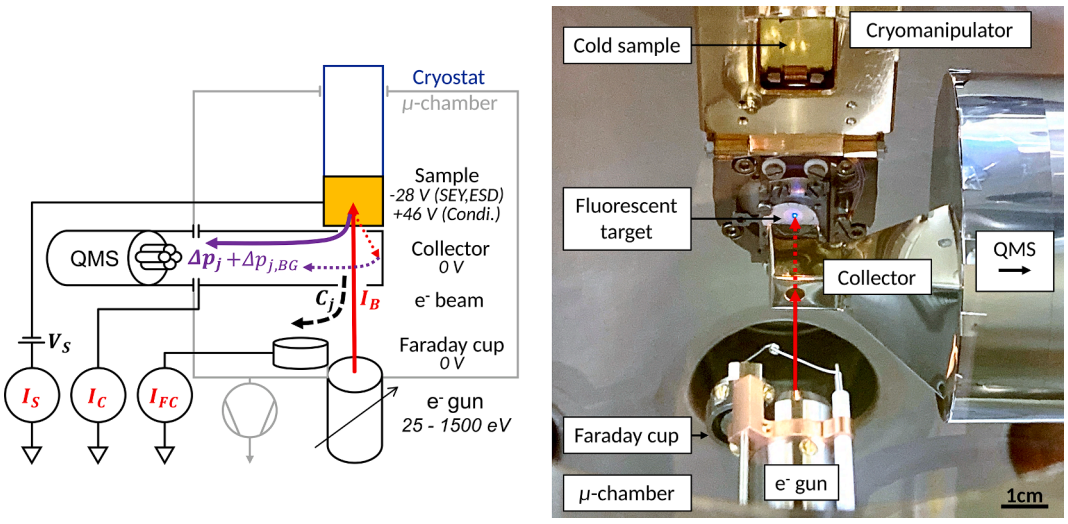

Fig. 1. Schematized arrangement for SEY and ESD yield measurements in the sub-keV region. See the text for detailed description.

and brings confidence in our electron current measurements.

The negative bias of $V_S = -28$ V imposed on the sample creates a retarding potential that decelerates the primary electron beam before impact. The potential gradient also repels the emerging secondary electrons away from the negatively biased sample towards the grounded collector, where they are measured as the collector current I_c. The scan across the energy spectrum is realized by incrementally ramping up the electron gun energy from 25 eV up to 1.4 keV, being the energy interval feasible in our arrangement. Doing so, the measurement of both SEY and ESD effectively starts from 0 eV electron kinetic energy as referenced to the vacuum level E_{vac} of the biased sample. When the kinetic energy of primary electrons lies below the electrostatic potential of the sample, the entire beam is reflected towards the collector, as measured in our setup and illustrated in Fig. 4. Once the kinetic energy surpasses the retarding potential, the primary electron beam begins interacting with the sample in various ways and all secondaries are recollected and sum up to the collector current I_C.

To obtain a uniform electron dose across the irradiated spot, we under-focused the electron beam from an originally Gaussian transverse profile (≈Ø1 mm) to a circular shape with an approximately flat-top profile. We first visually tuned the beam profile at different energies using a fluorescent target and then verified the transverse profile by cross–scanning it in two directions using a Ø 10 mm Faraday cup mounted on the cryomanipulator's rear side. To ensure that the probe beam fits into the conditioned spot, we used a Ø 3 mm wide beam spot (7.1 mm^2) for conditioning, but only Ø 2 mm wide beam (3.1 mm^2) to probe the ESD and SEY energy dependence. We also verified the spot size post-mortem by measuring the diameter of the discolored spot that appeared on the conditioned sample. The Fig. 2 schematizes the use of the knife edge scan technique for an e$^-$ beam profile measurement of a 260 eV beam spot. The FC current I_{FC} increases, as the beam gradually crosses the edge and enters the FC. Finally, the width of the ramp determines the beam size to be Ø 3 mm (6.5–3.5 mm) wide, as marked in the plot. The same result is obtained in both horizontal and vertical directions, marked X and Z.

Table 1 lists the typical electron beam parameters used in our measurements. The beam current used for a SEY measurement is about 0.5 nA and surpasses by a factor of 50 the dark current of the data acquisition electronics. A SEY measurement is considered non-destructive, as it does not desorb gas from the sample, nor does it chemically alter the surface. Conversely, an ESD scan over the feasible energy range (0–1.1 keV) is by definition destructive as the surface gas coverage is depleted.

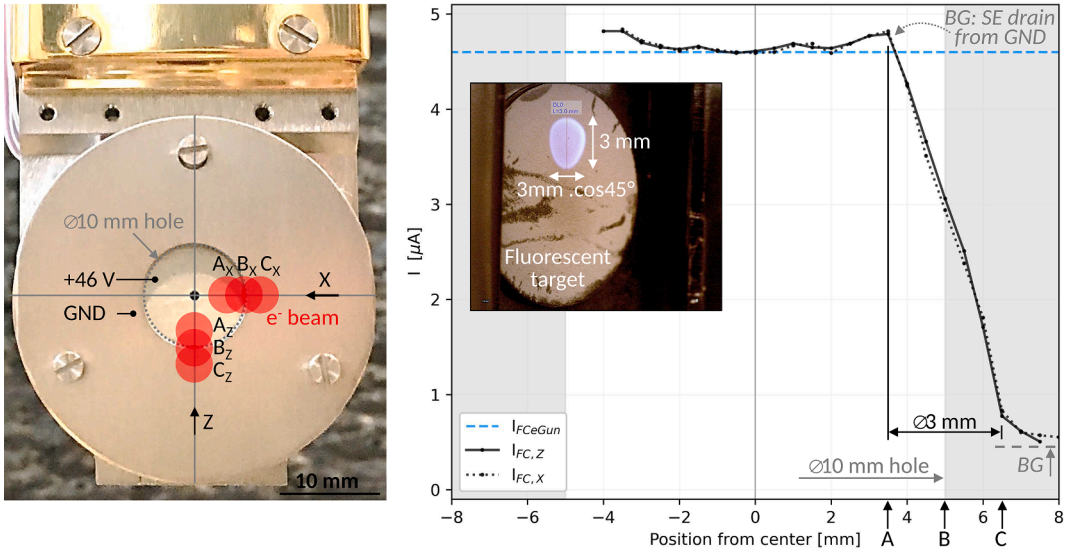

Fig. 2. Left: Cryomanipulator far side with concentric Faraday cups and annotations. Right: Scan of e$^-$ beam transverse profile in X and Z directions using a knife edge scan technique on the Ø 10 mm wide Faraday cup.

Table 1
Typical electron beam parameters used to measure the SEY and ESD energy dependence and for electron conditioning.

	I_B [A]	Spot diameter [mm]	Dose per measurement [C.mm^{-2}]	Dose per datapoint [C.mm^{-2}]	Time per measurement [min]
SEY energy scan	0.5nA	2	2.10^{-8}	2.10^{-10}	5
ESD energy scan	2 μA	2	7.10^{-5}	2.10^{-6}	5
Conditioning	~2μA	3	5.10^{-3}	–	90

Typically, a beam current in the μA range is necessary to generate a significant change in partial pressure of the studied gas species. In an effort to minimize the conditioning effect, i.e. electron dose per area imparted by an energy scan for ESD measurement, we minimize the irradiation time, the beam current and the number of datapoints. We also under-focus the beam to Ø 2 mm to increase the spot diameter, as compared to the focused ≈Ø 1 mm Gaussian profile. Besides that, most measured datapoints reside below 20 eV, as the datapoints are dense in this dynamic low-energy region and sparse above that. As a result, an ESD measurement with a dose in the mid 10^{-5} C.mm^{-2} range has a minor conditioning effect, which is limited, in the worst-case scenario, to some tens of % on an as-received surface. We verified that the curve preserves its shape when doing the energy scan in a reverse direction, hence ruling out a possible conditioning effect. We also obtain the same shape on a conditioned surface, where electron dose imparted by the energy scan can be neglected. Finally, we calculated a combined uncertainty of 10 % on the imparted dose per unit area. Indeed, the combined uncertainty is evaluated via the square sum of uncertainties weighted by the respective partial derivatives squared.

2.3. SEY measurement

In engineering practice, the SEY is defined as the average number of electrons emitted from the sample per incoming primary electron, regardless of the scattering mechanism. In our setup, the SEY can be directly evaluated from the currents measured on the collector and sample, which allows the acquisition of a full SEY curve during a single routine. This helps in avoiding uncertainties linked to the e- gun stability when the SEY is acquired in a two-step mode (e.g. when modifying the sample bias or inserting a Faraday cup to measure the primary electron beam). We estimate a combined uncertainty of about 5 % on the SEY value across the studied range.

The sample current I_S is a sum of arriving primaries and escaping secondaries. The SEY of the surface renders this net current either positive or negative. The collector current I_C contains all secondaries and is always positive. Normalizing the collector current I_C by the beam current I_B allows us to calculate the SEY, denoted δ, as follows in eq. (1):

$$\delta = I_{SE}/I_B = I_C/(I_S + I_C) \quad (1)$$

The SEY evolves with the primary energy and so do the relative proportions of reflected, backscattered and secondary electrons. The incoming electrons can either be elastically backscattered at the original energy, inelastically backscattered at an intermediate energy, or create true low-energy secondary electrons. The electron energy distribution of secondaries was calculated [26] and also measured [27] for the exact same technical-grade polycrystalline copper as in our present investigation. Reflected electrons, i.e. elastically backscattered, are predominant for primary energies below ~ 20 eV, and true secondary electrons dominate above.

We used a HOPG as a calibration reference to validate our current measurement method, which is crucial for SEY and ESD measurements. The HOPG sample with a 0.8° mosaic spread was air–cleaved and load–locked into the UHV, where it was conditioned by 300 eV electrons to remove the surface contaminant overlayer. The HOPG sample was not baked nor high temperature annealed. Fig. 2 shows the SEY curve measured on the HOPG sample and its inset zooms into the low-energy region.

The inset clearly shows the work function edge of the SEY curve, where the primary electrons just make it over the potential barrier of the studied surface. The sample current is nil below and non-zero above this value [28]. We used this edge as a reference to calibrate the energy scale and set the vacuum energy level $E_{vac} = 0$ eV, thereby excluding the work function and its possible changes from our studies. The exact position of 0 eV is verified for each sample in each run and used as a reference also for the ESD energy scans.

Above this edge, the SEY curve exhibits a fine structure across the studied energy range but is especially visible at energies below 40 eV. The ability to detect this fine structure substantiates the energy resolution we achieve with this setup. These findings, along with the peak value δ_{max} are in excellent agreement with the HOPG SEY measurements of Gonzalez, Cimino et al. [29,30] and Bellissimo et al. [31].

2.4. Desorbing gas flux measurement

When positioned at only 0.25 mm away from the studied sample, the collector also acts as a Feulner cap [32], directing the desorbed gas species towards the QMS positioned inside the collector. Hence, the desorbed species are analyzed before being pumped from the collector's inner volume through the geometry-restricted opening that is the only pumping port, i.e. with no additional pumping on the collector. The collector's closed geometry creates a conductance-limited system, which restricts the pumping speed, decouples the collector's inner volume from the heavily cryo-pumped chamber and invariably defines the pumping speed across all experiments and irrespective of possible variations. The differential pumping also rules out possible sample contamination by electron source degassing. Aside from the QMS, the collector houses a Bayard-Alpert Gauge (BAG) that only serves the described calibration purposes and is switched off during regular operation to reduce outgassing and prevent possible gas fragmentation, pumping, and a memory effect. A bakeout combined with electron conditioning of the inner surfaces ensures low thermal outgassing [33] and low stimulated gas desorption of the collector [34], further minimizing the residual gas background, as detailed in the next section. For completeness, the collector used here was recently redesigned towards the current Feulner cap style since our last publication [35]. This upgraded design enhanced the sensitivity of desorption measurements, for both ESD and Temperature Programmed Desorption (TPD), by more than 2 orders of magnitude by reducing the cryopumping of desorbed molecules onto the cryostat. Given the collector's geometrical proportions, cryopumping on the cold sample can only lead to an underestimation of the measured ESD yield by a factor of 2 in the upper limit. This factor is given by the ratio of pumping to cryopumping speeds, both given by the two 4 mm holes. We indeed observe this transient effect in the early stage of electron conditioning, and it is in line with the observations made by Anashin [36] and Malyshev [37].

The gas load Q_j [mbar.l.s^{-1}] of a species j desorbed in the collector is calculated from the known pumping speed of the collector C_j [l.s^{-1}], from the measured change in the QMS current Δi_j [A] and QMS absolute sensitivity k_j, [A.mbar^{-1}] to a gas j. Both the conductance and the QMS sensitivity are calibrated in-situ by a gas injection at room temperature, as follows.

To determine the collector conductance C_j, a constant flux Q_j of a single gas species is injected alternately through the collector conductance C_j or through a reference conductance $C_{j,ref}$ (not shown ins Fig. 1).

This reference conductance is calculated analytically, corrected for the Clausius factor and the result checked against a simulation. Since the flux Q_j is kept constant, the resulting pressure differences Δp_j and $\Delta p_{j,ref}$ are in the same proportion as the conductances C_j and $C_{j,ref}$. The H_2, CH_4, N_2 and Ar gases are injected to measure the conductance C_j as a function of molar mass M_j, uniformly covering the relevant mass/charge range from 2 m/q to 40 m/q. The measured conductances C_j are then fitted with a scaling factor inversely proportional to the molar mass $(1/M_j)^{1/2}$ to obtain a function of $C_j = f(M_j)$ used for gas load calculation. This calibration procedure for $C_j = f(M_j)$ results into a pumping speed of 21.8 ℓ/s for H_2 with a systematic uncertainty of ~20 % for all masses. Such approach provides a more robust estimate of the collector conductance than one would achieve by simply measuring and scaling the H_2 conductance by $(2/M)^{1/2}$ for heavier gases.

Since the QMS calibration is essential for partial pressure measurement of individual gas species present in the collector, we performed an in-situ calibration by injecting gases of interest, i.e. dominant residual gases: H_2, CO, and CH_4, C_2H_6 as well as N_2 and Ar. The absolute sensitivities for CO_2 and H_2O were adopted from ex-situ measurements due to their challenging nature. An ex–situ calibrated BAG served as an absolute pressure reference to determine the absolute sensitivity k_j of the Pfeiffer QMG700 QMS to a partial pressure of a gas species j. A gas injection creates a single gas-dominated atmosphere, that allows us to reference the QMS current reading at the corresponding mass/charge to the pressure read by the BAG, corrected for the relative sensitivity to N_2. The QMS sensitivity k_j is referenced to an ex-situ calibrated BAG (SVT type) that has an estimated 10 % uncertainty on the absolute pressure reading. We calculated a systematic uncertainty of QMS partial pressure p_j measurement of 20 %, induced by long-term variations, but considered constant throughout a run. The noise-induced statistical uncertainty is measured around 10 % for the partial pressure change Δp_j.

2.5. ESD yield derivation

The measured ESD yield $\eta_{e,j}$ of a given gas species j is calculated by dividing the gas flux of each desorbed gas species Q_j by the total electron flux impinging on the sample surface I_B/q_e, as seen in eq. (2). The flux of desorbing gas is calculated knowing the gas-dependent pumping speed $Q_j(M_j)$ and the partial pressure rise Δp_j measured by a calibrated QMS. The change in a partial pressure Δp_j is calculated as the change in QMS current Δi_j divided by the absolute sensitivity $k_j[A.mbar^{-1}]$ of the QMS to a given gas species j. The temperature T is estimated to be 300 K, as any desorbing gas quickly thermalizes in the room-temperature collector before reaching the QMS, hence no need to correct for thermal transpiration. The electron flux is obtained from the total current of the primary electron beam $I_B = I_C + I_S$ divided by the electron charge q_e. The input variables uncertainties propagate to about 30 % combined uncertainty at 1 σ confidence level for the calculated ESD yields across all relevant conditions. The statistical uncertainty contributes with about 10 % and leads to a repeatability and precision of the same magnitude.

$$\eta_{e,j} = \frac{C_j.\Delta i_j/k_j}{k_B.T}\Big/\frac{I_B}{q_e} + \frac{C_j.\Delta i_{j,BG}/k_j}{k_B.T}\Big/\frac{I_C}{q_e} \cong \frac{C_j.\Delta i_j/k_j}{k_B.T}\Big/\frac{I_B}{q_e} \quad (2)$$

The second term in the eq. (2) stands for the parasitic gas desorption originating from the collector's inner surface, which recollects reflected, backscattered, and true secondary electrons emitted by the sample. This irradiation creates a so-called 'dynamic background' that manifests as a non-zero value of ESD yield around 0 eV energy and below, where the molecular desorption threshold from the sample itself is nil (see Fig. 4). Since the dynamic background intensity scales linearly with the primary beam current I_B, it cannot be avoided by optimizing the beam current. Instead, we reduced this dynamic background by about one order of magnitude by electron conditioning the collector's inner surface. This was done by holding a dummy sample at –200 V with respect to the grounded collector and irradiating it with a high current and high energy primary beam. The reflected and secondary electrons escaping from the dummy sample effectively conditioned the stainless-steel surface of the collector in direct view of the sample. Following this procedure, the dynamic background is conditioned and currently limits our instrumental sensitivity to about 10^{-3} H_2 /e^- and 10^{-4} CO/e^-, depending on the biasing scheme. However, it is only a limiting factor for measuring highly conditioned metal surfaces with low ESD yields, typically around threshold energy and at high electron doses. In all other cases, i.e. above the threshold energy and at moderate electron doses, the strong signal from the high-yielding sample dominates over the dynamic background signal. The true ESD yield is then measured, as represented by the right term of eq. (2).

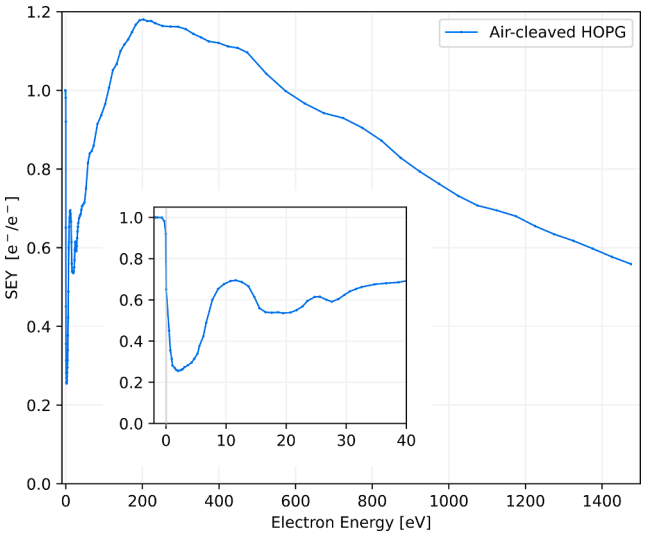

Fig. 3. SEY measured as a function of primary electron kinetic energy on an air-cleaved HOPG reference sample held at ambient temperature. The inset zooms into the low-energy region. The energy is referenced to the vacuum level.

2.6. ESD threshold derivation

The ESD yield energy dependence can be measured point-by-point at discrete values of primary electron energies. The top-left side in Fig. 4 plots a time series of square wave modulation of the beam current, as measured in the sample-collector system. Each peak is measured with incrementally larger primary electron energy. For this ESD measurement, the datapoints are spaced by 1 eV below 16 eV and progressively more above this low-energy region. The bottom-left side shows the QMS readout, which is also modulated in direct response to the electron beam. Each displayed datapoint is sampled during a 5 s long irradiation interval, allowing a stable QMS reading interleaved with a 5 s long idle time with no e^- beam to recover the background pressure and retune the e^- gun. We began with the QMS sampling through all channels at 1 Hz rate and later increased it to 10 Hz for higher temporal resolution at the cost of marginal noise increase. To speed up the acquisition time of an ESD energy scan, as well as to minimize the imparted electron dose, we later decreased the modulation period to 4 s and tuned down the beam current to units of μA. This optimized measurement routine is now automated in LabVIEW with postprocessing in Python to ensure reproducibility. As denoted for the QMS channel at 2 m/q, corresponding to H_2, the signal consists of a static background (1 nA) coming from the residual gas, then a dynamic background (0.25 nA) originating from the electron-irradiated collector, and finally, the signal from the sample itself that interests us.

To calculate the ESD yield, the static background is subtracted from all measured datapoints, as denoted by the Δi_j in Eq. (2). Only the dynamic component is kept, illustrating the detection limit imposed by the dynamic background. Hence, the right side of Fig. 4 plots the 'uncorrected' ESD yield is for $^{15}N_2$, H_2 and CO as a function of the primary

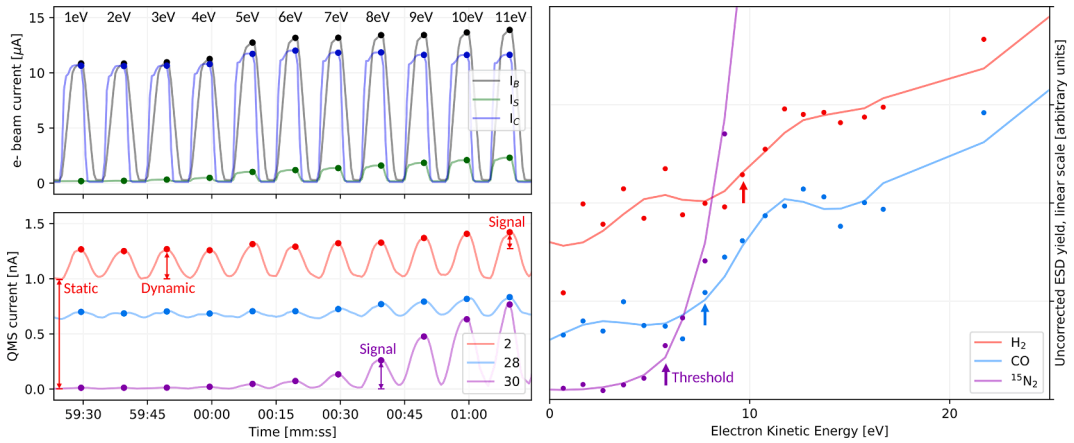

Fig. 4. Low-energy ESD yield measurement of partly conditioned copper surface held at 15 K with a 1 ML precoverage of $^{15}N_2$ used as a tracer. Top-left: Time series of e^- beam, sample and collector currents, all modulated to a square wave. The kinetic energy is incremented by 1 eV each cycle. Bottom-left: QMS currents for 2, 28 and 30 m/q modulated in response to the e^- beam current. Right: Datapoints and S-G smoothed trendlines for H_2, CO and $^{15}N_2$ yields as a function of primary e^- kinetic energy. Arrows mark the desorption threshold energies for each gas. Note the noise and dynamic background levels of $^{15}N_2$ compared to H_2 and CO.

electron kinetic energy referenced to the sample. To capture the approximative trendline behind the scattered datapoints, we used a Savitzky-Golay (S-G) smoothing filter [38], that effectively removes noise while preserving detail of the dynamics behind it.

We used an isotopically labelled $^{15}N_2$ as a tracer gas to commission this measurement method by obtaining an easily and unambiguously interpretable data. A thin pre-coverage of $^{15}N_2$ (1 monolayer, ML) was quench–condensed over the semi-conditioned copper substrate held at 15 K. The gas dose equivalent to a 1ML coverage was determined by analysing a series of TPD curves, a method described earlier[35]. The sample is then irradiated with electrons of increasing energy that would eventually surpass the energy threshold and start desorbing the cryosorbed $^{15}N_2$. As opposed to the $^{14}N_2$ that resides at a highly polluted peak 28 m/q of a residual gas spectrum, the $^{15}N_2$ isotope resides at a peak 30 m/q, which is a clean channel with little natural background. This makes our $^{15}N_2$ signal clearly distinguishable from the static and dynamic backgrounds, so the desorption threshold can be clearly identified. We measured the threshold energy for the $^{15}N_2$ desorption to be around 6 eV. This corresponds to Rakhovskaia's [39] measurement for a 50 ML thick N_2 coverage that gives 7.6 eV, referenced to the vacuum level. This is reasonably close to our result and the observed difference can be either a sensitivity limitation imposed by the dynamic background or a substrate-related effect linked to a single- versus multilayer coverage regime.

Despite the 1 ML-thick adsorbate overlayer, the electron beam interacts with the copper substrate, desorbing the hereafter studied H_2 and CO. The noisy and elevated background renders it difficult to identify the signal coming from the copper sample, but, knowing what to look for, the same threshold behaviour can also be identified for H_2 and CO. The dynamic background maintains a quasi-constant value across this low-energy region. Once the primary electron energy surpasses the desorption threshold, the ESD yield rises about linearly with energy and ultimately the signal of the high-yielding sample rapidly dwarves the background. To locate the threshold energy, one can characterize the dynamic background by its mean value and standard deviation. The threshold can be defined as the first datapoint that surpasses the background's mean value and standard deviation. Indeed, this experimental approach works well for relatively high-yielding samples but cannot detect energy thresholds below this noisy background. Following this method, one can estimate the energy threshold for H_2 to be around 9 eV and 8 eV for CO, as indicated in Fig. 4 and discussed in detail in Section 3.2.

We carried out a series of complementary measurements to support the correctness of our threshold identification from our experimental data. First, we tested the energy threshold moves accordingly when imposing a small variation to the sample's retarding bias. Second, we dosed multilayer pre-coverages of other gases, such as $^{15}N_2$, CH_4 and Ar over Cu and Au substrates, to verify that these cryosorbed gases exhibit similarly high yields and low energy thresholds around 10 eV and irrespective of the used substrate. Further tests performed with as-received copper samples held at ambient temperatures did not show any measurable difference in the energy thresholds as compared to the cryogenic conditions. These experiments unambiguously link the desorbing $^{15}N_2$ gas, and by extension other gases, to the source at the cold sample, demonstrating that the chosen experimental approach is correct and provides valid and reproducible data in agreement with the literature.

3. Results and discussion

With the presented experimental methods, we obtained the following results for an unbaked as-received OFE copper surface held at 15 K, sampled from an industrially produced LHC sheet. All measurements, i.e. electron conditioning, ESD and SEY energy scans, were performed at 15 K. Each electron conditioning and subsequent ESD and SEY energy scan was measured on a previously intact spot of the same copper sample. The sample was heated to 100 K and cooled back down to 15 K before each ESD measurement to desorb gases that could cryosorb from the residual gas background. For clarity, we commence with measurements of SEY energy dependence and its dependence on electron irradiation. We then add energy scans of ESD yields for the same conditioning states. Finally, we investigate the influence of temperature on ESD yields when going from ambient to cryogenic temperatures.

3.1. SEY measurement

We measured the SEY curves of each surface state before and after each electron irradiation, see Fig. 5 The as-received surface state of the LHC-grade copper again serves as the baseline, having a high $\delta_{max} = 2.9$ located at $E_{max} = 250$ eV.

First, we measured that 300 eV electron irradiation most effectively decreases the SEY curve across the entire studied energy range. Electron dose of $8.4 .10^{-4}$ C.mm^{-2} conditions the SEY to a peak value $\delta_{max} = 1.1$, a value below the multipacting threshold in dipoles, quadrupoles and field-free regions in the LHC that have thresholds of 1.3, 1.1 and 1.5, respectively. A similar dose of 1 keV electrons only conditioned the SEY to $\delta_{max} = 1.25$, but further irradiation proved that 1 keV can also decrease the SEY to $\delta_{max} = 1.1$. Furthermore, 1 keV irradiation does not

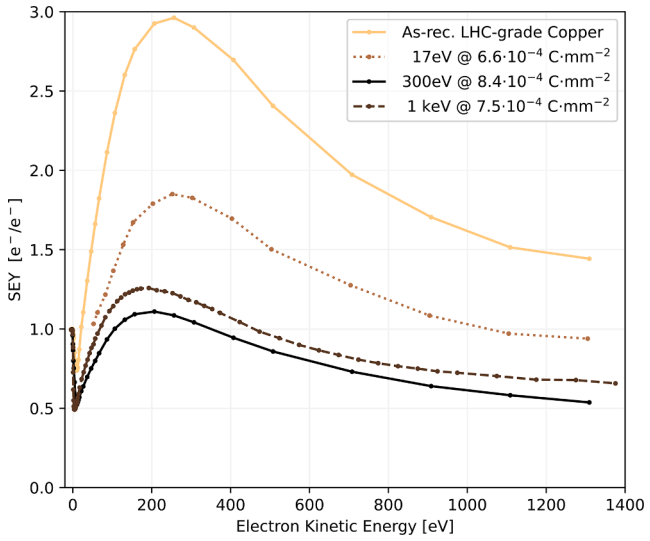

Fig. 5. SEY of a Cu surface held at 15 K as a function of primary electron kinetic energy and surface state. Note that the effective SEY decreases when conditioned with 300 eV and 1 keV instead of a limited conditioning effect of 17 eV electron irradiation.

condition proportionally faster than 300 eV, but is less performant instead. This, along with the general shape of SEY curve, suggest that it is the near-surface true secondary electrons responsible for the conditioning effect.

Irradiation with 17 eV electrons at this moderate dose manifested as a limited decrease of SEY to $\delta_{max} = 1.8$. The slight decrease seems to be linked to a limited removal of contaminants. As for the peak position E_{max} on the energy axis is shifted from 250 eV to about 200 eV when conditioned with 300 eV and 1 keV, but remains unchanged after the 17 eV irradiation. Note that the HOPG from Fig. 3, representing a graphitic surface, peaks out around $E_{max} = 200$ eV. The inability to approach $\delta_{max} = 1.1$ and no E_{max} decrease both point to the lack of graphitization of surface contaminants when irradiated with 17 eV electrons. Increasing the 17 eV electron dose up to a 5 mC.mm^{-2} does bring a more tangible conditioning effect, achieving $\delta_{max} \approx 1.5$, but never reaches the ultimate efficacy of higher energy electron irradiation.

Our SEY measurements taken at cryogenic temperatures correspond with the results presented in literature, typically taken at ambient temperature. We observe the same effect as, Nishiwaki [40], or Scheuerlein [41], who linked the SEY decrease to surface graphitization and Cimino et al. [42,43], who demonstrated the limited conditioning effect of low-energy electrons. Our experimental observations agree with the general understanding of SEY conditioning developed at ambient temperatures and seen as well at cryogenic conditions by Cimino et al. [27]. More SEY curves taken at ambient and cryogenic temperature were published for technical-grade Cu, Al and SS [44], which exhibit similarly positioned E_{max} but different δ_{max}. Though these results are inconclusive due to an unspecified surface state in terms of e$^-$ conditioning and cryosorbate precoverage.

3.2. ESD yield energy dependence

We then studied the energy dependence of H_2 and CO ESD yields in the 0–1.1 keV energy range using the measurement procedure and data analysis detailed above. Similarly to SEY scrubbing, the primary electron energy plays a major role in the ESD conditioning. Fig. 6 shows H_2 and CO yields measured as a function of primary electron energy for an unbaked LHC–grade copper in several conditioning states. Other gases, such as CO_2 and CH_4 were also measured and exhibit the same general behaviour but are not depicted for simplicity. The ESD curves were first measured for an as-received surface state and then again after irradiation with an electron dose of ~7.10^{-4} C.mm^{-2} at energies of 17 eV, 300 eV and 1 keV. The discrete scattered datapoints are smoothed with an S-G filter to facilitate reading the general trend. To illustrate the statistical uncertainty of the measurement, we plot the raw datapoints around the smoothed curve of the as–received state.

This investigated energy range contains the following regions of interest for H_2 and CO. We will discuss these regions separately and also interpret the acquired data in the framework of the IMGR model [45–47] as Desorption Induced by Electronic Transitions (DIET).

First, it is the desorption threshold, where the ESD yield of each gas rises significantly above the dynamic background once the primary electron energy surpasses the threshold energy necessary to trigger the desorption. As the initial step of the gas desorption process, the electronic transition brings about a threshold behaviour that we observed for both physisorbed and chemisorbed gas species. We measured the threshold energies around 6 eV for cryosorbed $^{15}N_2$, and higher for chemisorbed gases: 8 eV for CO and 9 eV for H_2. This indeed agrees with the theoretical framework, as stronger-bound species should have higher thresholds and lower yields. The threshold energy lies just under 10 eV, remarkably close to the anecdotal '10-Volt effect' from Redhead's memoirs [48]. Besides this, the only closest dataset is that of Billard et al. [49], who measured desorption from a technical-grade copper surface at ambient temperature and only extrapolated towards the low energy. Their extrapolated energy threshold lies in the 10 eV region for both H_2

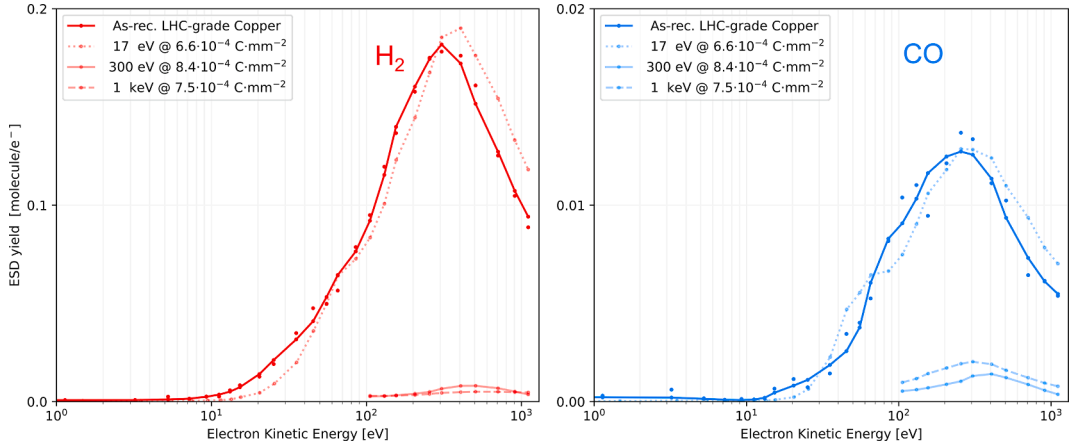

Fig. 6. H_2 (left) and CO ESD yields for LHC-grade copper surface held at 15 K at different conditioning states measured as a function of primary electron energy. Datapoints measured on an as-received Cu are scatter-plotted around the smoothed curve to illustrate the statistical uncertainty. Mind the log x-scale to capture the low energy region and different vertical scales for H_2 and CO.

and CO, which compares well to our values. There is no other available data regarding the low-energy ESD from unbaked technical-grade metals, especially at cryogenic temperatures.

Beyond the energy threshold, the ESD yield increases monotonically until about 300 eV, where the ESD yield peaks out. In this energy region, the ESD yield is proportional to the net energy deposited by the primary electrons within the electron escape depth, i.e. 'close' to the surface and therefore available to stimulate desorption. The primary electron energy is deposited in electronic excitations that may further dissipate by triggering either electron or molecular emission, manifesting as SEY or ESD phenomena. This common origin places the peaks at about the same energy for both ESD and SEY curves. Once more, the experimental observations support the DIET interpretation.

As the primary electron energy increases, the energy deposition depth also increases, and fewer electronic excitations reach the surface to promote gas desorption (or secondary electron emission). We have recently illustrated this argument in detail for the case of thick adsorbate layers [35]. Consequently, the ESD yield either levels off or even peaks out at few hundreds of eV.

When further increasing the primary energy, the peak is followed by a slow decay with a generic $1/E^n$ energy dependence, as the energy deposition depth penetrates deeper into the bulk [50], below the escape depth of electronic excitations [51]. Such general behaviour was also measured for technical copper by Achard [52] in an open–geometry experimental arrangement similar to ours. By contrast, Malyshev devised a closed-geometry experiment [53], more similar to an actual beam–screen, and measures a knee, where others detect a peak, followed by only a less steep increase at few hundreds of eV. This dissonance of results taken in different experimental arrangements is to be better understood.

As for the electron conditioning effect, i.e. ESD decrease during extended electron irradiation, the exposure to 300 eV and 1 keV electrons efficiently scrubs off gas prone to desorption and gradually decreases the ESD yield across the investigated energy range. The result of conditioning strongly varies when comparing the conditioning effect of 17 eV, 300 eV and 1 keV electron irradiation. A moderate dose of 300 eV and 1 keV electron effectively reduced the yield across the investigated energy range by a factor of 20 for H_2 yield and the CO yield by about a factor of 5. It is worth noting here that 1 keV irradiation does not condition proportionally faster when compared to 300 eV, similarly to what is observed for SEY. As opposed to 300 eV and 1 keV, irradiation with 17 eV electrons had no measurable effect on the ESD yield at this moderate electron dose and needs to be further investigated at much higher doses. The limited conditioning effect of low-energy electrons was indeed observed for ESD yield of stainless steel at ambient temperatures by Malyshev et al. [53] and is in line with observations made on SEY of copper by Cimino et al. Hence, the primary electron energy significantly influences the electron conditioning efficiency.

3.3. ESD yield temperature dependence

Since the cryomanipulator allows active control of the sample temperature, we also investigated the ESD yield temperature dependence between 15 K and 265 K, see Fig. 7 The transition to cryogenic temperatures strongly influences the ESD yield as measured on another as-received copper sample irradiated by 300 eV electrons. Notably, ESD yields of all followed gasses decreased at cold on average by a factor of 10, with the sole exception of CO_2 yield which plummeted by 2 decades. No hysteresis or conditioning was observed, as the same ESD yields were measured during a cool-down and warm-up phase. When decreasing the temperature, the ESD yield drops first for heavier molecules, such as H_2O, and at lower temperatures for lighter ones, such as H_2. However, the molar mass alone does not explain all the variability.

This measurement suggests that the ESD yield's limiting step is the recombination rate and/or surface mobility, which are both strongly temperature-dependent. This phenomenon is to be studied better to understand the origin of this decrease at low temperatures. A similar trend was observed by Baglin and Jenninger in COLDEX [54], when exposing a semi-conditioned copper BS to a synchrotron radiation of 194 eV critical energy while varying the temperature from ambient down to 5 K. The PSD yield from the studied technical-grade copper had notably similar behaviour, i.e. also dropped at cryogenic temperatures by a similar factor as we observed here for the ESD. This is no coincidence, as the DIET theory also encompasses the PSD, as practically illustrated by Schumann et al. [55].

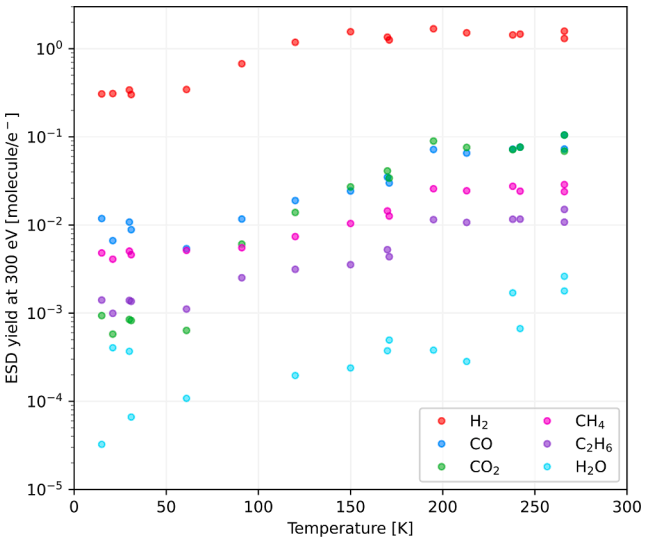

Fig. 7. Temperature dependence of ESD yield as measured at 300 eV energy on an as-received LHC-grade copper surface.

4. Summary and conclusions

We have designed and commissioned an experimental approach to measure the SEY and ESD yield of metal surfaces held at cryogenic conditions, in order to investigate the low-energy electron irradiation of LHC-grade copper beam screen material held at cryogenic temperatures. This includes the ESD yield evolution with energy and temperature, measurement of the desorption threshold energy, and assessing the scrubbing efficiency of different electron energies.

To reach this objective, we use a combination of a low-energy monochromatic electron source and a retarding sample bias, which enables the study of the 0–1.4 keV energy range. In combination with electron conditioning of the dynamic background, a newly designed molecular collector in a Feulner cap style [31] increased our experimental sensitivity to 10^{-3} H_2/e^- range. We used a Highly Oriented Pyrolytic Graphite as a reference sample to validate the SEY measurement against existing data. We then used an isotopically labelled $^{15}N_2$ cryosorbed onto the copper sample, which enabled us to discriminate the signal from static and dynamic backgrounds, thus validating the low-energy ESD measurement. The newly commissioned setup delivers reproducible results in agreement with the general understanding of the problematics and comparable data, whether for SEY [27,43] or ESD yields, thresholds and conditioning [52,49,56].

With this new instrument at hand, we present the first direct laboratory measurement of ESD yield in the sub–keV energy range of LHC-grade copper held at a temperature of 15 K. We demonstrated that the post-irradiation ESD yield and SEY both strongly depend on the primary electron energy used for irradiation, as shown for 17 eV, 300 eV and 1 keV at doses around 7.10^{-4} C.mm^{-2}. The presented data further demonstrates that the electron conditioning equally works at cryogenic temperatures in a manner similar to ambient temperatures and drives the SEY below the multipacting limit of LHC quadrupoles $\delta_{max} < 1.1$. We then substantiate the importance that surface temperature has on the

ESD yield by varying temperatures between from 265 K to 15 K and back.

Our experimental results are particularly relevant for understanding the relation between the electron cloud activity and the dynamic vacuum effect systematically observed in LHC's cryogenic beam tube during Run 1 [1,10,13–17] and Run 2 [18,19], or other accelerators operating at cryogenic temperature [57], including the future ones [3,4,6,7]. Considering that the energy spectrum of an electron cloud lies mostly below the desorption threshold [24], the data we present can be used to better understand the dynamic vacuum effect or optimize the beam-scrubbing strategy toward faster conditioning rates [58]. Insofar, our experimental data indicate that the beam scrubbing effect can be partly attributed to the decrease of SEY and partly to the ESD yield decrease, also in the cryogenic temperature region that was previously uncharted. We also demonstrated that the primary electron energy is of major importance in this low-energy region and needs further investigation. Therefore, we intend to continue the research to refine the understanding of ESD problematics for various technical-grade metal surfaces taken under a range of environmental and irradiation conditions.

CRediT authorship contribution statement

Michal Haubner: Data curation, Formal analysis, Investigation, Methodology, Software, Visualization, Writing – original draft, Writing – review & editing. **Vincent Baglin:** Conceptualization, Funding acquisition, Methodology, Project administration, Writing – review & editing. **Bernard Henrist:** Conceptualization, Methodology, Resources.

Declaration of Competing Interest

The authors declare that they have no known competing financial interests or personal relationships that could have appeared to influence the work reported in this paper.

Data availability

Data will be made available on request.

Acknowledgements

The authors thankfully acknowledge the support of CERN's TE-VSC group, its workshop, and N. Kos for providing the LHC-grade samples.

The corresponding author's work was partly supported by the Ministry of Education, Youth and Sports of the Czech Republic [Czech Technical University in Prague project SGS21/149/OHK2/3T/12] and by the HL-LHC Project.

References

[1] V. Baglin, G. Bregliozzi, G. Lanza, J.M. Jimenez. Synchrotron radiation in the LHC vacuum system (No. CERN-ATS-2011-245). URL: epaper.kek.jp/IPAC2011/papers/tups019.pdf. 2011.

[2] W. Fischer, M. Blaskiewicz, M. Brennan, H. Huang, H.C. Hseuh, V. Ptitsyn, ... U. Iriso. Electron cloud observations and cures in RHIC. In 2007 IEEE Particle Accelerator Conference (PAC) (pp. 759-763). IEEE. https://doi.org/10.1103/PhysRevSTAB.11.041002. 2007.

[3] S.Y. Zhang. eRHIC Beam Scrubbing, BNL-114220-2017-IR, June 2017, Brookhaven National Laboratory, Upton, NY, United States. https://doi.org/10.2172/1392223.

[4] G. Rumolo, I. Hofmann, E. Mustafin, O. Boine-Frankenheim. Vacuum and electron cloud issues at the GSI present and future facilities. Proc. of ECLOUD'04: 31st advanced ICFA beam dynamics workshop on electron-cloud effect,. 2005, Napa, CA, USA, (pp. 95-101). https://doi.org/10.5170/CERN-2005-001.95.

[5] M. Benedikt, et al., FCC-ee: the lepton collider, Eur. Phys. J. Special Top. 228 (2) (2019) 261–623, https://doi.org/10.1140/epjst/e2019-900045-4.

[6] M. Benedikt, et al., FCC-hh: the hadron collider, Eur. Phys. J. Special Top. 228 (4) (2019) 755–1107, https://doi.org/10.1140/epjst/e2019-900087-0.

[7] The CEPC-SPPC Study Group, CEPC-SppC Preliminary Conceptual Design Report, Vol II: Accelerator, IHEP-CEPC-DR-2015-01, March 2015. URL: https://cepc.ihep.ac.cn/preCDR/Pre-CDR_final_20150317.pdf.

[8] O. Brüning, et al. LHC Design Report. CERN-2004-003, June 2004, Geneva, Switzerland. https://doi.org/10.5170/CERN-2004-003-V-1.

[9] O. Gröbner, Overview of the LHC vacuum system, Vacuum 60 (1–2) (2001) 25–34, https://doi.org/10.1016/S0042-207X(00)00240-2.

[10] F. Zimmermann (2002). Electron cloud effects in the LHC. https://doi.org/10.5170/CERN-2002-001.47.

[11] S. Berg. Energy gain in an electron cloud during the passage of a bunch (No. LHC-Project-Note-97). CERN-LHC-Project-Note-97. URL: https://cds.cern.ch/record/692004.

[12] G. Arduini, V. Baglin, E. Benedetto, R. Cimino, P. Collier, I. Collins, ... & F. Zimmermann. Present understanding of electron cloud effects in the Large Hadron Collider. In Proceedings of the 2003 Particle Accelerator Conference (Vol. 3, pp. 1727-17s29). IEEE. URL: https://cds.cern.ch/record/620194. 2003.

[13] G. Rumolo, N. Mounet, C. Zannini, Arduini, et al. Electron cloud observations in LHC (No. CONF, pp. 2862-2864), Proc. of IPAC'11, Sept 2011, San Sebastian, Spain. URL: https://jacow.org/IPAC2011/papers/THOBA01.pdf. 2011.

[14] G. Bregliozzi, V. Baglin, P. Chiggiato, P. Cruikshank et al. Observations of electron cloud effects with the LHC vacuum system, Proc. of IPAC'11, September 2011, San Sebastian, Spain. paper TUPS018, pp. 1560-1562. URL: https://jacow.org/IPAC2011/papers/TUPS018.pdf.

[15] G. Lanza, V. Baglin, G. Bregliozzi, J. M. Jimenez. LHC Beam vacuum during 2011 machine operation, Proc. of IPAC'12, May 2012, New Orleans, Louisiana, USA. URL: https://jacow.org/IPAC2012/papers/WEPPD018.pdf.

[16] G. Lanza, V. Baglin, G. Bregliozzi, J.M. Jimenez. LHC vacuum system: 2012 review and 2014 outlook, Proc. of LHC beam operation workshop - Evian 2012, December 2012, CERN-ATS-2013-045, Geneva, Switzerland. URL: https://cds.cern.ch/record/2302432.

[17] V. Baglin, G. Bregliozzi, G. Lanza, J.M. Jimenez. Vacuum performance and lessons for 2012, Proc. of Chamonix 2012 workshop on LHC performance, CERN-2012-006, Geneva, Switzerland. https://doi.org/10.5170/CERN-2012-006.74.

[18] E. Buratin, V. Baglin, B. Henrist, P. Chiggiato, A. Fasoli, Electron flux and pressure dynamic in the LHC vacuum pilot sector as a function of beam parameters and beam pipe properties, Phys. Rev. Accelerators Beams 23 (11) (2020), 114802, https://doi.org/10.1103/PhysRevAccelBeams.23.114802.

[19] C.Y. Vallgren, P.R. Metidieri, G. Bregliozzi. Beam induced dynamic pressure during Run 2 (2015-2018): Machine operation in the LHC. In CERN Yellow Reports: Conference Proceedings (Vol. 7, pp. 65-65). https://doi.org/10.23732/CYRCP-2020-007.65. 2020.

[20] V. Baglin, The LHC vacuum system: commissioning up to nominal luminosity, Vacuum 138 (2017) 112–119, https://doi.org/10.1016/j.vacuum.2016.12.046.

[21] High-Luminosity Large Hadron Collider (HL-LHC): Technical Design Report Ed. by I. Bejar Alonso, O. Brüning, P. Fessia, M. Lamont, L. Rossi, L. Tavian, M. Zerlauth. CERN 2020-10, CERN, Geneva, Switzerland. https://doi.org/10.23731/CYRM-2020-0010.

[22] R. Cimino, T. Demma, Electron cloud in accelerators, Int. J. Modern Phys. A 29 (17) (2014) 1430023.

[23] G. Iadarola. Electron cloud studies for CERN particle accelerators and simulation code development (Doctoral dissertation, CERN). URL: https://cds.cern.ch/record/1705520/. 2014.

[24] E. Buratin. Electron Cloud and Synchrotron Radiation characterization of technical surfaces with the Large Hadron Collider Vacuum Pilot Sector (Doctoral dissertation, CERN). EPFL. URL: https://cds.cern.ch/record/2746058. 2020.

[25] A.G. Mathewson. The effects of cleaning and other treatments on the vacuum properties of technological materials used in ultra high vacuum. Vuoto, Scienza e Tecnologia, 17(3) 1987 102-116. URL: https://cds.cern.ch/record/183509.

[26] J. Cazaux, Reflectivity of very low energy electrons (<10 eV) from solid surfaces: physical and instrumental aspects, J. Appl. Phys. 111 (6) (2012), 064903, https://doi.org/10.1063/1.3691956.

[27] R. Cimino, I.R. Collins, Vacuum chamber surface electronic properties influencing electron cloud phenomena, Appl. Surface Sci. 235 (1–2) (2004) 231–235, https://doi.org/10.1016/j.apsusc.2004.05.270.

[28] R. Cimino, L.A. Gonzalez, R. Larciprete, A. Di Gaspare, G. Iadarola, G. Rumolo, Detailed investigation of the low energy secondary electron yield of technical Cu and its relevance for the LHC, Phys. Rev. ST Accel. Beams 18 (5) (2015), 051002, https://doi.org/10.1103/PhysRevSTAB.18.051002.

[29] L.A. Gonzalez, R. Larciprete, R. Cimino, The effect of structural disorder on the secondary electron emission of graphite, AIP Adv. 6 (9) (2016), 095117, https://doi.org/10.1063/1.4963644.

[30] R. Cimino, M. Angelucci, L.A. Gonzalez, R. Larciprete, SEY and low-energy SEY of conductive surfaces, J. Electron Spectrosc. Relat. Phenomena 241 (2020), 146876, https://doi.org/10.1016/j.elspec.2019.06.008.

[31] Bellissimo, Alessandra, et al. Secondary electron generation mechanisms in carbon allotropes at low impact electron energies. J. Electron Spectrosc. Relat. Phenomena 241 (2020): 146883. https://doi.org/10.1016/j.elspec.2019.07.004.

[32] P. Feulner, D. Menzel, Simple ways to improve ''flash desorption'' measurements from single crystal surfaces, J. Vacuum Sci. Technol. 17 (2) (1980) 662–663.

[33] V. Nemanič, J. Setina, Outgassing in thin wall stainless steel cells, J. Vacuum Sci. Technol. A: Vacuum, Surfaces, Films 17 (3) (1999) 1040–1046, https://doi.org/10.1116/1.581680.

[34] O.B. Malyshev, B.T. Hogan, M. Pendleton. Effect of surface polishing and vacuum firing on electron stimulated desorption from 316LN stainless steel. J. Vacuum Sci. Technol. A: Vacuum, Surfaces, Films, 32(5) 2014 051601. DOI: https://doi.org/10.1116/1.4887035.

[35] R. Dupuy, M. Haubner, B. Henrist, J.H. Fillion, V. Baglin, Electron-stimulated desorption from molecular ices in the 0.15–2 keV regime, J. Appl. Phys. 128 (17) (2020), 175304, https://doi.org/10.1063/5.0021832.

[36] V.V. Anashin, O.B. Malyshev, I.R. Collins, O. Gröbner. Photon-stimulated desorption and the effect of cracking of condensed molecules in a cryogenic vacuum system. Vacuum, 60(1-2) 2001 15-24. https://doi.org/10.1016/S0042-207X(00)00239-6.
[37] O.B. Malyshev. Vacuum in Particle Accelerators: Modelling, Design and Operation of Beam Vacuum Systems. John Wiley & Sons. 2020. https://doi.org/10.1002/9783527809134.
[38] A. Savitzky, M.J. Golay, Smoothing and differentiation of data by simplified least squares zprocedures, Analyt. Chem. 36 (8) (1964) 1627–1639, https://doi.org/10.1021/ac60214a047.
[39] O. Rakhovskaia, P. Wiethoff, P. Feulner, Thresholds for electron stimulated desorption of neutral molecules from solid N_2, CO, O_2 and NO, Nucl. Instrum. Methods Phys. Res. B Nucl. Instrum. Meth. B 101 (1–2) (1995) 169–173, https://doi.org/10.1016/0168-583X(95)00296-0.
[40] M. Nishiwaki, S. Kato, Graphitization of inner surface of copper beam duct of KEKB positron ring, Vacuum 84 (5) (2009) 743–746, https://doi.org/10.1016/j.vacuum.2009.06.028.
[41] C. Scheuerlsein, M. Taborelli, N. Hilleret, A. Brown, M.A. Baker, An AES study of the room temperature conditioning of technological metal surfaces by electron irradiation, Appl. Surf. Sci. 202 (1–2) (2002) 57–67, https://doi.org/10.1016/j.vacuum.2009.06.028.
[42] R. Larciprete, D.R. Grosso, M. Commisso, R. Flammini, et al., Secondary electron yield of Cu technical surfaces: dependence on electron irradiation, Phys. Rev. Special Top.-Accelerators Beams 16 (1) (2013), 011002, https://doi.org/10.1103/PhysRevSTAB.16.011002.
[43] R. Cimino, M. Commisso, D.R. Grosso, T. Demma, V. Baglin, R. Flammini, R. Larciprete, Nature of the decrease of the secondary-electron yield by electron bombardment and its energy dependence, Phys. Rev. Lett. 109 (6) (2012), 064801, https://doi.org/10.1103/PhysRevLett.109.064801.
[44] J. Fang, Y. Hong, S. Wang, Y. Wang, B. Zhu, W. Zhang, B. Bian, Y. Wang, Cryogenic secondary electron yield measurements on structural materials applied in particle accelerators, Nucl. Instrum. Methods Phys. Res. Sect. A: Accelerators, Spectrometers, Detectors and Associated Equipment 1027 (2022) 166292, https://doi.org/10.1016/j.nima.2021.166292.
[45] Y. Isikawa, 51. The desorption of the adsorbed hydrogen on a platinum plate by the impact of slow electrons, Proc. Imperial Acad. 18 (5) (1942) 246–250, https://doi.org/10.2183/pjab1912.18.246.
[46] D. Menzel, R. Gomer, Desorption from metal surfaces by low-energy electrons, J. Chem. Phys. 41 (11) (1964) 3311–3328, https://doi.org/10.1063/1.1725730.
[47] P.A. Redhead, Interaction of slow electrons with chemisorbed oxygen, Can. J. Phys. 42 (5) (1964) 886–905, https://doi.org/10.1139/p64-083.
[48] P.A. Redhead, The first 50 years of electron stimulated desorption (1918–1968), Vacuum 48 (6) (1997) 585–596, https://doi.org/10.1016/S0042-207X(97)00030-4.
[49] F. Billard, N. Hilleret, G. Vorlaufer. Some results on the electron induced desorption yield of OFHC copper. Vacuum Technical Note 00-32, CERN. https://doi.org/10.17181/CERN.9UX2.OKJV. 2000.
[50] K.A. Kanaya, S. Okayama, Penetration and energy-loss theory of electrons in solid targets, J. Phys. D: Appl. Phys. 5 (1) (1972) 43, https://doi.org/10.1088/0022-3727/5/1/308.
[51] Q. Gibaru, C. Inguimbert, M. Belhaj, M. Raine, D. Lambert, Monte-Carlo simulation and analytical expressions for the extrapolated range and transmission rate of low energy electrons [10 eV–10 keV] in 11 monoatomic materials, Appl. Surf. Sci. 570 (2021), 151154, https://doi.org/10.1016/j.apsusc.2021.151154.
[52] M.H. Achard (1976). Desorption des gaz induite par des electrons et des ions de l'acier inoxydable, du cuivre OFHC, du titane et de l'aluminium purs, CERN-ISR-VA-76-34, CERN, Geneva, Switzerland. CM-P00064839. URL: https://cds.cern.ch/record/314507.
[53] O.B. Malyshev, et al., Electron stimulated desorption from the 316 L stainless steel as a function of impact electron energy, J. Vacuum Sci. Technol. A: Vacuum, Surfaces, Films 31 (3) (2013), 031601, https://doi.org/10.1116/1.4798256.
[54] V. Baglin, I.R. Collins, O. Gröbner, C. Grünhagel, B. Jenninger, Molecular desorption by synchrotron radiation and sticking coefficient at cryogenic temperatures for H_2, CH_4, CO and CO_2, Vacuum 67 (3–4) (2002) 421–428, https://doi.org/10.1016/S0042-207X(02)00226-9.
[55] M. Andritschky, O. Gröbner, A.G. Mathewson, F. Schumann, P. Strubin, R. Souchet, Synchrotron radiation induced neutral gas desorption from samples of vacuum chambers, Vacuum 38 (8–10) (1988) 933–936, https://doi.org/10.1016/0042-207X(88)90495-2.
[56] K. Kennedy. Electron stimulated desorption rates from candidate vacuum chamber surfaces. LBL, Berkeley, July 1986. DOI: 10.2172/1872213 URL: https://www.osti.gov/biblio/1872213/.
[57] S.Y. Zhang, L. Ahrens, J. Alessi, M. Bai, et al. Experience in reducing electron cloud and dynamic pressure rise in warm and cold regions in RHIC, Proc. of EPAC 2006, June 2006, Edinburgh, Scotland. URL: https://www.osti.gov/biblio/885019.
[58] O. Bruning, F. Caspers, I.R. Collins, O. Grobner, B. Henrist, N. Hilleret, ... X. Zhang. Electron cloud and beam scrubbing in the LHC. In Proceedings of the 1999 Particle Accelerator Conference (Cat. No. 99CH36366) (Vol. 4, pp. 2629-2631). IEEE. URL: https://cds.cern.ch/record/386682. 1999.